

## Article

# Uncertainties and Perspectives on Forest Height Estimates by Sentinel-1 Interferometry

Samuele De Petris , Filippo Sarvia  and Enrico Borgogno-Mondino 

Department of Agriculture, Forestry and Food Science, University of Torino, L.go Braccini 2, 10095 Grugliasco, Italy; filippo.sarvia@unito.it (F.S.); enrico.borgogno@unito.it (E.B.-M.)

\* Correspondence: samuele.depetris@unito.it

**Abstract:** Forest height is a key parameter in forestry. SAR interferometry (InSAR) techniques have been extensively adopted to retrieve digital elevation models (DEM) to give a representation of the continuous variation of the Earth's topography, including forests. Unfortunately, InSAR has been proven to fail over vegetation due to low coherence values; therefore, all phase unwrapping algorithms tend to avoid these areas, making InSAR-derived DEM over vegetation unreliable. In this work, a sensitivity analysis was performed with the aim of properly initializing the relevant operational parameters (baseline and multilooking factor) to maximize the theoretical accuracy of the height difference between the forest and reference point. Some scenarios were proposed to test the resulting "optimal values", as estimated at the previous step. A simple model was additionally proposed and calibrated, aimed at predicting the optimal baseline value (and therefore image pair selection) for height uncertainty minimization. All our analyses were conducted using free available data from the Copernicus Sentinel-1 mission to support the operational transfer into the forest sector. Finally, the potential uncertainty affecting resulting height measures was quantified, showing that a value lower than 5 m can be expected once all user-dependent parameters (i.e., baseline, multilooking factor, temporal baseline) are properly tuned.

**Keywords:** Sentinel-1; SAR; interferometry; phase unwrapping avoiding; forest height; uncertainty assessment; topographic levelling approach



**Citation:** De Petris, S.; Sarvia, F.; Borgogno-Mondino, E. Uncertainties and Perspectives on Forest Height Estimates by Sentinel-1 Interferometry. *Earth* **2022**, *3*, 479–492. <https://doi.org/10.3390/earth3010029>

Academic Editor: Charles Jones

Received: 1 March 2022

Accepted: 17 March 2022

Published: 18 March 2022

**Publisher's Note:** MDPI stays neutral with regard to jurisdictional claims in published maps and institutional affiliations.



**Copyright:** © 2022 by the authors. Licensee MDPI, Basel, Switzerland. This article is an open access article distributed under the terms and conditions of the Creative Commons Attribution (CC BY) license (<https://creativecommons.org/licenses/by/4.0/>).

## 1. Introduction

Forest height is a key parameter in forestry since it is adopted to retrieve above ground biomass [1,2] and characterized canopy vertical structure [3–5]. It is often used to detect forests [6], and to assess forest ecosystem services (e.g., timber production [7], forest protection capabilities against natural hazards [8], biodiversity [9,10]). Forest height is ordinarily measured through ground campaigns by means of hypsometers, with precision ranging between 1 and 3 m [11,12]. Unfortunately, ground surveys are time and cost consuming, making them poorly dense over forested areas. Conversely, remote sensing can fill this gap, providing continuous forest height measures over wide areas, and showing accuracy comparable to ground surveys [13].

Space-borne Earth Observation missions fit forest requirements well, making it possible to map and monitor wide areas, allowing near-early change detection and a frequent updating of forest properties [14]. Synthetic aperture radars (SARs) are known to be useful for estimating forest geometric features when recording data in all-weather condition, including equatorial/tropical climates, where clouds almost constantly cover the forest. Among SAR application and methods, the SAR interferometry (InSAR) technique has been extensively adopted to generate digital elevation models (DEM) intended to provide a continuous representation of Earth topography, including forest areas. Theoretically speaking, radar interferometry can generate highly precise height estimates related to the differences of path length between scattered signals received by two properly positioned

antennas. The ordinary InSAR processing workflow relies on a phase unwrapping step aimed at unambiguously recovering the local topography, which is generally achieved by unitarily processing the entire scene. Ordinarily, these algorithms tend to avoid these areas during unwrapping [15,16], so the approach has proven to consistently fail where signal coherence values are low. This makes InSAR-derived DEM over vegetation highly unreliable [17].

An alternative existing approach, not widely explored in the literature [18–20], is considered in this work for obtaining more reliable and accurate estimates of forest height from InSAR data by avoiding phase unwrapping. This method changes the working paradigm from a mapping problem involving the entire scene to a local paradigm based on the comparison between a forest pixel interferogram and a reference one closely located outside the forest. Specifically, the potentialities and limitations of such an approach are explored and discussed.

In this work, with reference to the above-mentioned approach, a sensitivity analysis was also performed with the aim of properly initializing the relevant operational parameters (i.e., baseline and multilooking factor) to maximize the theoretical accuracy of height measures. To support the technological transfer, all the analyses were made with reference to SAR open data (guaranteeing a cost-effective data access) with a specific focus on the Copernicus Sentinel-1 (S1) mission.

## 2. Materials and Methods

Given the above-mentioned goals of this work, the analysis was performed according to the workflow of Figure 1. The first step was to develop a reasonable model to estimate forest height and define the conditions in which it can be adopted (see Section 2.2, Interferometric Phase Modelling). The second step was to model the theoretical uncertainty of the estimates (see Section 2.3, Modelling  $dh$  Uncertainty). The third step to tune the involved parameters to optimize the operational conditions for minimizing the uncertainty of forest height estimates (see Section 2.4, Minimizing  $\sigma_{dh}$  through simulated scenarios). All simulations were performed according to Sentinel-1 data.

### 2.1. Sentinel 1 Data

Satellite missions, such as the European Union (EU) Copernicus Sentinels, generate a significant volume of data that may be proficiently used to aid the support of environmental studies and land management. Nevertheless, technological transfer, presently, appears to be limited, even if web-based services based on these data are becoming operational [21–23]. In the general context of satellite open data, SAR imagery shows a further weakness in entering operational services mainly due to the complexity of data processing [24,25] and data availability.

S1 is one of the current largest space-borne missions providing free and open accessible SAR data. Furthermore, the European Space Agency (ESA) has made the free software SNAP (Sentinel Application Platform) available for users, enabling an easier and focused exploitation of products from the Copernicus Programme [17,26]. The S1 mission is a two-satellite constellation (Sentinel-1A and Sentinel-1B) acquiring a microwave C-band (5.6 cm wavelength). Its main acquisition mode over land is the interferometric wide swath (IW) recording backscattered signal in dual pole mode (VV and VH). Data are natively recorded as complex values (I/Q components) and in-SAR geometry (range and azimuth). In particular, its medium–high spatial resolution and high revisit time (6 days) make S1 mission useful for a wide range of applications, including forest mapping.

In the literature, many methods based on SAR interferometry have been proposed to estimate forest height and can be summarized into three main categories: (a) the Pol-InSAR methodology [27–29]; (b) coherence-based methodology [30–32]; and (c) interferometric phase-based methodology [19,20]. Unfortunately, S1 data are not suitable for (a) due to the lack of quad-pol channels that would be required [21,33]. Approach (b) is mainly applied using tandem acquisition mode that guarantees a higher coherence over vegetation. Since

S1 does not support tandem acquisition, coherence values over forests are generally low, limiting this approach. Consequently, approach (c) appears to be the most promising, because it is somehow consistent with the technical features of S1 data. S1 main technical features [34–37] are reported in Table 1, and used for the following simulations.

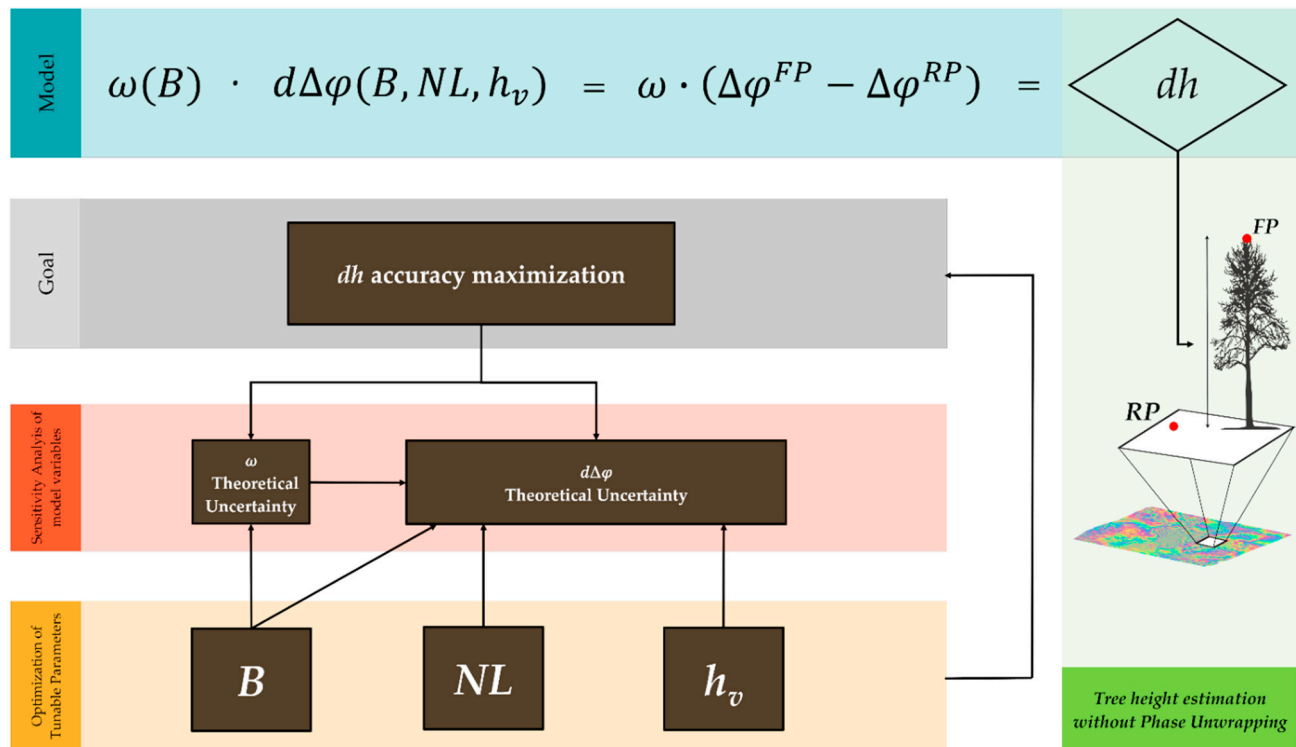


**Figure 1.** Workflow adopted in this work.  $B$  is the baseline;  $NL$  is the interferogram multilooking factor;  $h_v$  is the expected average forest height;  $dh$  is the estimated forest height according to proposed model;  $\Delta\phi^{FP}$  and  $\Delta\phi^{RP}$  are the interferometric phases of a forest point and a reference (ground) point, respectively;  $\omega$  is the gain factor that allows the conversion of an interferometric phase difference ( $d\Delta\phi$ ) into height difference.

**Table 1.** S1 mission nominal features.

Feature	Values	Units
Frequency ( $\lambda$ )	5.54	cm
Nominal Satellite Altitude (H)	693	km
Look Angle ( $\theta$ )	30–45	°
Attitude accuracy ( $\sigma_\theta$ )	0.01	°
Maximum Noise Equivalent Sigma Zero (NESZ)	−22	dB
Spatial resolution range ( $\delta_{rg}$ )	5	m
Spatial resolution azimuth ( $\delta_{az}$ )	20	m
Satellite position accuracy POD	5	cm
Bandwidth ( $Bw$ )	42–56	MHz
Antenna real length ( $L$ )	12	m

## 2.2. Interferometric Phase Modelling

SAR interferometry relies on image pairs processing acquired from different positions separated by a proper distance known as a baseline ( $B$ ). This condition makes it possible to recover “stable” object height through a simple geometric transformation [38–40]. Unfortunately, this technique is known to suffer from many limitations in vegetated areas, mainly due to the noise induced by canopy volume and interferometric signal decorrelation.

Assuming a flattened interferogram with no significant ground shifts affecting the area, the contribution to the interferometric phase ( $\Delta\varphi$ ) given by local topography can be defined according to Equation (1):

$$\frac{d\Delta\varphi}{dh} = \frac{4\pi B}{\lambda R \tan \theta} = k_z = \frac{1}{\omega} \quad (1)$$

where  $\Delta\varphi$  is the interferometric phase;  $h$  is the target point elevation;  $\lambda$  is the wavelength of the radar signal;  $R$  is the sensor-target slant range;  $\theta$  is the antenna off-nadir angle (look angle);  $B$  is the baseline; and  $\omega$  is the gain factor needed to convert back a phase difference into the correspondent height difference.

Inverting Equation (1), the height difference ( $dh$ ) between the two compared points can be obtained by Equation (2). This approach appears to be similar to an ordinary topographic levelling problem [41]. Subsequently, forest point absolute elevation can be obtained by adding  $dh$  to at least one reference point (representing the ground) having known elevation:

$$dh = h^{FP} - h^{RP} = \omega (\Delta\varphi^{FP} - \Delta\varphi^{RP}) \quad (2)$$

where  $h^{FP}$  and  $\Delta\varphi^{FP}$  are elevation and interferometric phase of the forest point, respectively, and  $h^{RP}$  and  $\Delta\varphi^{RP}$  are elevation and interferometric phase of the reference point, respectively. It is worth noting that Equation (2) can be retained phase unwrapping independent if the expected forest height is maintained lower than the so called height of ambiguity (HOA) [19,30].

This condition is satisfied if no significant elevation difference exists between forest and reference ground levels. This condition can be a priori-verified using an external DEM (e.g., global SRTM or ASTER DEMs). The condition must be tested for each interferogram pixel to remove inadequate ones. HOA can be obtained multiplying  $2\pi$  to  $\omega$ , and it is possible to model the relationship between HOA and  $B$ .

### 2.3. Modelling $dh$ Uncertainty

Once the above-mentioned condition has been satisfied, one can proceed to estimate the expected uncertainty of  $h^{FP}$ , taking care of the contribution of the involved parameters.  $h^{FP}$  uncertainty ( $\sigma_{dh}$ ) can be estimated by Equations (3) and (4), assuming  $h^{RP}$  uncertainty as a priori known. Equation (3) is the one commonly adopted in the literature to estimate  $\sigma_{dh}$  [42]:

$$\sigma_{dh} = \omega \cdot \sigma_{d\Delta\varphi} \quad (3)$$

where  $\sigma_{dh}$  is  $dh$  uncertainty and  $\sigma_{d\Delta\varphi}$  is the interferometric phase difference uncertainty.

It is worth highlighting that this formula does not consider for  $\omega$  uncertainty; this has to be further considered to properly model error propagation that can be proficiently estimated by the Variance Propagation Law (VPL, [43]). VPL is a statistical tool (Equation (4)) useful to estimate the a priori variance of a statistical variable ( $y$ ) depending on some other independent ones ( $x_i$ ):

$$\sigma_y^2 = \left( \frac{\partial y}{\partial x_1} \right)^2 \cdot \sigma_{x_1}^2 + \left( \frac{\partial y}{\partial x_2} \right)^2 \cdot \sigma_{x_2}^2 + \dots + \left( \frac{\partial y}{\partial x_n} \right)^2 \cdot \sigma_{x_n}^2 \quad (4)$$

where  $y = f(x_1, x_2, \dots, x_n)$  is the dependent variable,  $x_i$  the independent one, and  $\sigma_{x_n}^2$  their variance (supposed to be known).

Application of VPL to Equation (3) results in Equation (5):

$$\sigma_{dh} = \sqrt{\left( \frac{\partial dh}{\partial \omega} \sigma_\omega \right)^2 + \left( \frac{\partial dh}{\partial d\Delta\varphi} \sigma_{d\Delta\varphi} \right)^2} \quad (5)$$

where  $\sigma_\omega$  and  $\sigma_{d\Delta\varphi}$  are the expected uncertainties for  $\omega$  and  $d\Delta\varphi$ , respectively.

### 2.3.1. Theoretical Uncertainty of $\omega$

$\omega$  uncertainty ( $\sigma_\omega$ ) depends on the parameters involved in its computation. Again, the variance propagation law can be used to obtain the estimate of the theoretical value of  $\sigma_\omega$  (Equation (6)):

$$\sigma_\omega = \sqrt{\left(\frac{\partial\omega}{\partial B}\right)^2 \cdot \sigma_B^2 + \left(\frac{\partial\omega}{\partial R}\right)^2 \cdot \sigma_R^2 + \left(\frac{\partial\omega}{\partial\theta}\right)^2 \cdot \sigma_\theta^2 + \left(\frac{\partial\omega}{\partial R} \frac{\partial\omega}{\partial\theta}\right) \rho_{(R,\theta)} \sigma_R \sigma_\theta} \quad (6)$$

where  $R$  is the slant range (here computed as  $R = \frac{H}{\cos\theta}$ );  $\sigma_B$  is the baseline uncertainty;  $\sigma_R$  and  $\sigma_\theta$  are the slant and look angle uncertainty, respectively;  $\rho_{(R,\theta)}$  is the Pearson's correlation coefficient between  $R$  and  $\theta$ . These are known to be geometrically related (thus correlated), and consequently  $\rho_{(R,\theta)}$  must be set to +1.

Concerning  $\sigma_B$ , the S1-declared positional accuracy of the ESA provided precise orbit state vectors (Precise Orbit Determination—POD) is 5 cm [35,36]. This determines a  $\sigma_B$  value of 12 cm.  $\sigma_\theta$  was assumed equal to  $0.01^\circ$ , and that is the nominal antenna attitude accuracy.  $\sigma_R$  can be estimated by Equation (7), assuming factors contribution as additive:

$$\sigma_R = \sqrt{\sigma_{tropo}^2 + \sigma_{iono}^2 + \sigma_{proc}^2 + \sigma_{TOF}^2} \quad (7)$$

where  $\sigma_{tropo}$  and  $\sigma_{iono}$  are the uncertainty of atmospheric delay induced by troposphere and ionosphere;  $\sigma_{proc}$  is the estimated contribution of SAR data processing effects in the S1 IW products;  $\sigma_{TOF}$  is the uncertainty of slant range signal time, i.e., the minimum detectable slant range distance between two scatterers.

In order to evaluate the relative contribution of factors to the final estimate of  $\sigma_\omega$ , “weights” of Table 2 ( $w_i$ ) were computed with reference to  $\sigma_\omega^2$  according to Equation (6).

**Table 2.** “Weights” defining the relative importance of factors to determine  $\sigma_\omega^2$ .

Parameter	$w_i$ Formula
Baseline ( $B$ )	$w_B = \frac{\left(\frac{\partial\omega}{\partial B}\right)^2 \cdot \sigma_B^2}{\sigma_\omega^2}$
Slant range ( $R$ )	$w_R = \frac{\left(\frac{\partial\omega}{\partial R}\right)^2 \cdot \sigma_R^2}{\sigma_\omega^2}$
Look angle ( $\theta$ )	$w_\theta = \frac{\left(\frac{\partial\omega}{\partial\theta}\right)^2 \cdot \sigma_\theta^2}{\sigma_\omega^2}$
Mixed term ( $R, \theta$ )	$w_{corr(R,\theta)} = \frac{\left(\frac{\partial\omega}{\partial R} \frac{\partial\omega}{\partial\theta}\right) \cdot \rho_{(R,\theta)} \sigma_R \sigma_\theta}{\sigma_\omega^2}$

### 2.3.2. Theoretical Uncertainty of $d\Delta\varphi$

The theoretical uncertainty of  $d\Delta\varphi$  ( $\sigma_{d\Delta\varphi}$ ) can be computed by Equation (8):

$$\sigma_{d\Delta\varphi} = \sqrt{\sigma_{\Delta\varphi FP}^2 + \sigma_{\Delta\varphi RP}^2} \quad (8)$$

where interferometric phase uncertainties,  $\sigma_{\Delta\varphi FP}$ , and  $\sigma_{\Delta\varphi RP}$  were proved [18,44,45] to be strictly correlated to the local coherence magnitude,  $|\gamma|$ , according to Equation (9):

$$\sigma_{\Delta\varphi} = \frac{1}{\sqrt{2NL}} \frac{\sqrt{1 - |\gamma|^2}}{|\gamma|} \quad (9)$$

where  $NL$  is the multilooking factor (i.e., number of pixels used to compute the complex multilooked interferogram).

These considerations drive to admit that  $\sigma_{dh} = f(\omega, \sigma_{\Delta\varphi})$  and, consequently, they depend on the operational parameters  $B$  and  $NL$ .

Equations (1) and (3) show that  $dh$  accuracy is higher for long baselines. This is what is ordinarily reported in the literature. Nevertheless, this condition appears to fail over

vegetation. In fact, longer baselines decrease coherence, thus negatively affecting  $\sigma_{\Delta\varphi}$  and, consequently,  $\sigma_{d\Delta\varphi}$ . This effect is more evident while analysing the decorrelation model of Equation (10), as proposed by [44,46]. This model defines the coherence magnitude as the product of several contributions related to decorrelation agents.

$$\gamma_{obs} = \gamma_{thermal} \cdot \gamma_{Doppler} \cdot \gamma_{temp} \cdot \gamma_{geom} \cdot \gamma_{vol} \quad (10)$$

where  $\gamma_{obs}$  is the observed coherence magnitude;  $\gamma_{thermal}$  is the signal decorrelation due to additive thermal noise [47];  $\gamma_{Doppler}$  accounts for non-perfect overlap of the azimuth spectra for the master and slave SAR acquisitions and misregistration error [48];  $\gamma_{temp}$  is associated to changes in the dielectric and structural proprieties of the target [49];  $\gamma_{geom}$  depends on geometric relationships between the two compared SAR acquisitions; and  $\gamma_{vol}$  is the decorrelation component due to canopy scattering from multiple heights within each scattering cells.

Because  $\gamma_{thermal}$ ,  $\gamma_{Doppler}$ ,  $\gamma_{temp}$  are independent from any operational parameter that can be controlled by users, these were not taken into consideration in the optimization process addressed by authors in [50].

Differently,  $\gamma_{geom}$  is dependent from baseline according to Equation (11):

$$\gamma_{geom} = 1 - \frac{2 B \cos^2 \theta \delta_{rg}}{\lambda R} \quad (11)$$

where  $\delta_{rg}$  is the range resolution of the radar.

Similarly,  $\gamma_{vol}$  has to be taken into consideration, since this is caused by the volumetric decorrelation related to the vegetation canopy volume (distributed scatters). Assuming a uniform volume showing an exponential extinction of absorption and scattering,  $\gamma_{vol}$  can be modelled by Equation (12) ([18,49,50]). It states that SAR signal decorrelation depends on vegetation volume depth  $h_v$  (i.e., tree height) and from the system parameter  $k_z$  (see Equation (1)).

$$\gamma_{vol} = \frac{2 \sin\left(k_z \frac{h_v}{2}\right)}{k_z h_v} \quad (12)$$

Equation (12) assumes a uniform radar backscatter cross section from canopy volume and no significant scattering from the background. By inverting Equation (12), it would be possible to estimate forest height if decorrelation was caused entirely by volumetric effects. Unfortunately, this is unrealistic due to canopy signal attenuation, scattered movements, and the proportion of area filled by trees. These issues determine significant observational errors [50] making this approach with S1 data a poor choice.

Within this framework and according to the above-mentioned simplifications, a new synthetic variable  $\gamma_{baseline} = \gamma_{geom} \cdot \gamma_{vol}$  can be considered as directly related to the baseline value.

#### 2.4. Minimizing $\sigma_{dh}$ through Simulated Scenarios

As demonstrated in the previous sections,  $\sigma_{dh}$  depends on both  $\omega$  and  $\sigma_{\Delta\varphi}$ . While trying to minimize it, the only parameters a user can manage are image pair selection (spatial and temporal baseline) and the multilooking factor ( $NL$ ). These can be optimized to guarantee the lowest  $\sigma_{dh}$ .

Concerning the temporal baseline selection, since forests are continuously changing, the longer the temporal baseline, the lower the associated coherence (temporal decorrelation) [17,51]. Therefore, short temporal baseline and winter acquisitions are more suitable for forest height retrieval as discussed by [19,31,51]; however, currently, no formalized model exists to support this evidence.

As far as baseline optimization (i.e.,  $B$  value minimizing  $\sigma_{dh}$ ) is concerned, this must be managed going back to Equations (3), (11) and (12). These make it possible to generate different scenarios depending on varying baseline and  $h_v$  values (i.e., expected average forest



height). With reference to the scenarios, the optimal  $B$  value can be retrieved once an expected forest  $h_v$  is set. To make the estimate more immediate, a power model (Equation (13)) was calibrated directly relating  $h_v$  with the optimal  $B$  value:

$$B_{opt} = a \cdot (h_v)^b. \quad (13)$$

where  $a$  and  $b$  are model parameters.

Concerning  $NL$  value optimization, one has to consider Equation (5) that relates  $NL$  with  $\sigma_{\Delta\phi}$ : the higher  $NL$ , the lower the interferometric phase uncertainty.  $NL$  can therefore be optimized by fixing an expected value for  $\sigma_{dh}$  once  $\omega$  and local coherence are known (Equation (14)).

$$NL = 0.5 \left( \frac{1}{\gamma^2} - 1 \right) \left( \frac{\sigma_{dh}}{\omega} \right)^2 \quad (14)$$

According to Equation (14), after setting an expected  $\sigma_{dh}$ , the correspondent  $NL$  value can be obtained. To make this information more operational,  $NL$  can be easily translated into the correspondent squared pixel size (SGRP) by Equation (15). This works under the condition that the ratio between azimuth and range pixel size is the one of S1, i.e., 1:4 (see Table 1).

$$SGRP (m) = \frac{\delta_{az} \cdot \sqrt{NL}}{2} \quad (15)$$

Considering that the accuracy of forest height by ground survey is lower than 3 m, in this work some simulations retrieving SGRP at  $\sigma_{dh} = 3$  m were performed by changing the  $\gamma$  value between 0.1 and 1 in Equations (14) and (15). This makes it possible to find an optimal value of  $NL$  suitable to guarantee the expected accuracy of forest estimates.

Once optimal  $B$  and  $NL$  (or SGRP) values corresponding to an expected  $h_v$  were found, that part of  $\sigma_{dh}$ , depending on settable operational parameters, can be finally minimized.

Unfortunately, a significant part of  $\sigma_{dh}$  additionally depends on systematic errors such as orbital-related ones, flattening residuals and atmospheric delays. These cannot be directly accounted for, because they are difficult to model. Nevertheless, one can try to remove/minimize them by considering height differences between neighbour targets in place of absolute height measures. Measure differencing is expected to reasonably remove these errors, assuming that they occur similarly for close points [42].

Conversely, remaining error components depending on targets attributes, i.e., temporal decorrelation and random noise, cannot be further removed or minimized.

Their joint effect on the final uncertainty of  $dh$ , described in Equation (5), can be evaluated through simulations based on a sensitivity analysis approach.

These were achieved by differencing a reference ground point, external to the forest, and showing a very high coherence value ( $\geq 0.8$ ) with one representing the forest itself. The analysis proceeded by progressively varying the coherence value of the forest point ( $\gamma_{FP}$ ) from 0.05 to 1 and assuming different  $dh$  values with expected tree heights ranging between 1 m and HOA.

### 3. Results and Discussion

To verify if  $dh$  values associated with tree heights could be reasonably estimated independently from phase unwrapping, HOA was related to  $B$  according to the above-mentioned equations, namely  $HOA = 2\pi \cdot \omega$  and Equation (1).  $B$  values were progressively changed to generate graphs of Figure 2.

With reference to Figure 2, one can deduce that a baseline value lower than about 120 m can be used to ensure that forest height estimates can be given. In fact, forests around the world rarely show tree heights higher than 100 m. If focusing on temperate forests where maximum tree height is 65 m, baseline values lower than about 270 m can be used, ensuring to remain within HOA.

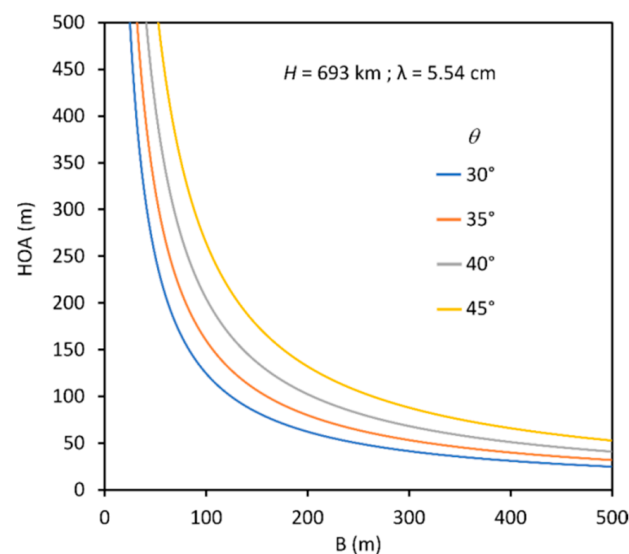


**Figure 2.** Maximum detectable  $dh$  (HOA), avoiding phase unwrapping, versus  $B$  and  $\theta$  (simulation performed with reference to S1 nominal features).

### 3.1. Theoretical Uncertainty of $\omega$

$\omega$  is the parameter that converts the interferometric phase difference (radians) into the correspondent height difference (meters,  $dh$ ).  $\omega$  uncertainty ( $\sigma_\omega$ ) depends both on the  $B$ ,  $R$ ,  $\theta$  factors value and on their accuracy (Equation (6)).

Concerning  $\sigma_B$ , it was obtained considering the S1-declared positional accuracy of the ESA provided POD, i.e., 5 cm [35,36]. A reference value for  $\sigma_B$  was found to be equal to 12 cm.  $\sigma_\theta$  was assumed equal to  $0.01^\circ$ , corresponding to the nominal antenna attitude accuracy for S1.  $\sigma_R$  was determined according to Equation (7).  $\sigma_{tropo}$  and  $\sigma_{iono}$  were set to 4 m and 1 m, respectively, according to [52]. This was obviously an approximation, since atmospheric conditions can locally change. The same paper [52] reported 0.4 m as a reference value for  $\sigma_{proc}$ .  $\sigma_{TOF}$  was set equal to 3.3 m, assuming that S1  $Bw$  (see Table 1) was 46 MHz.

According to the above-mentioned values,  $\sigma_R$  was finally computed (Equation (7)) resulting in 5.3 m.

To investigate  $\sigma_\omega$  dependency from involved parameters, one has to take care that  $R$  and  $\theta$  change along the scene, while  $B$  and  $H$  could be assumed constant. Measuring errors affecting these system parameters (Equation (1)) necessarily affect  $\sigma_\omega$ . VPL can be used to explore how  $B$  and  $\theta$  affect the theoretical value of  $\sigma_\omega$  (Equation (6)). Figure 3a shows that for  $B$  values greater than 50 m,  $\sigma_\omega$  was lower than 10 m and increased while  $\theta$  values increased (i.e., tending to the swath far range). These findings raise some doubts about Equation (3), which does not take into account the error contributions of the system parameters. Additionally,  $\sigma_\omega$  appeared to be highly significant. A better estimate of  $\sigma_{dh}$  could come from Equation (4) where, differently from Equation (3),  $\sigma_\omega$  is considered.

In order to explore the importance of system parameters on  $\sigma_\omega$ , correspondent weights ( $w_i$ ) were computed according to equations reported in Table 2. Results are reported in Figure 3b where it can be noted that 64%, 11% and 24% of the total variance ( $\sigma_\omega^2$ ) were due to the look angle,  $R$  and the mixed term accounting for  $R$  and  $\theta$  correlation, respectively.  $B$  uncertainty participated for less than 1%.

From an operational point of view, a rough sensitivity analysis can help to interpret results. For example, a look angle difference of  $1^\circ$  determines a  $\Delta\omega$  of about +3.7%; a satellite altitude difference of 10 km determines a  $\Delta\omega$  of about +1.4%; a slant range difference of 10 km determines a  $\Delta\omega$  of about +1.2%.  $\theta$  appears to be the most conditioning factor for  $\omega$  computation.



Given these values,  $\omega$  can be reasonably computed directly using the coarse estimates of  $\theta$ ,  $R$ ,  $H$ , and  $B$ , as reported in the SAR metadata information or satellite-approximated state vectors.

While using S1 nominal features in Equation (6), it can be easily derived that  $\sigma_\omega$  varies between 1 m to 10 m, thus demonstrating to significantly contribute to the interferometric-derived  $dh$ .

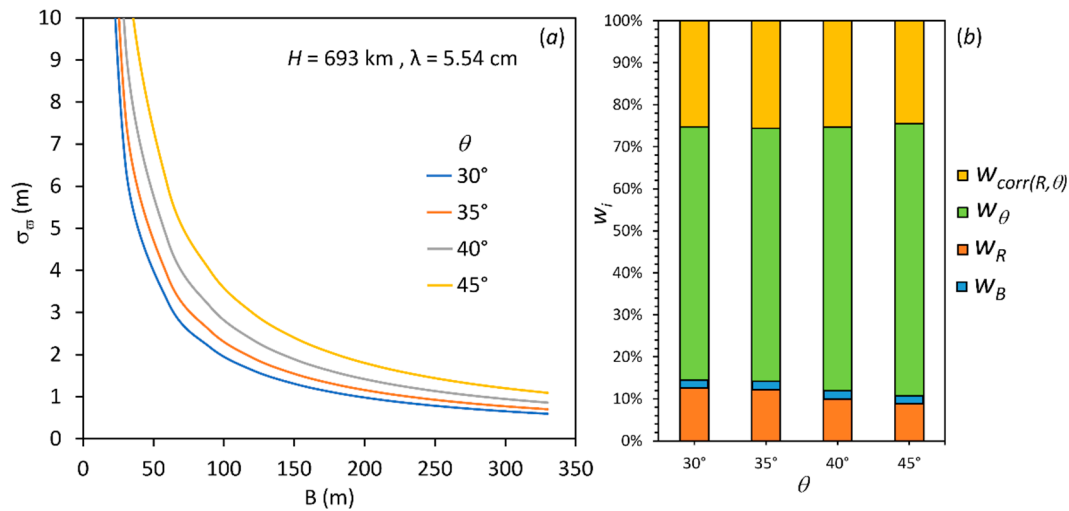


**Figure 3.** (a)  $\sigma_\omega$  versus  $B$  and  $\theta$ . (b) relative weights affecting  $\omega$  variance involved in VPL. Note that  $w_B$  is exaggerated by a factor 200.

### 3.2. Theoretical Uncertainty of $d\Delta\varphi$

According to Equations (11) and (12), some simulations were performed to explore the relationship between the baseline and  $\gamma_{geom}$  and  $\gamma_{vol}$  using S1 nominal values of Table 1 (Figure 4a,b). Figure 4a shows that expected forest height (i.e., the thickness of forest volume) does not significantly affect  $\gamma_{vol}$  if  $B$  is maintained lower than 50 m. Differently, for  $B$  values  $> 50$  m,  $h_v$  participates to reduce  $\gamma_{vol}$ . Figure 4b shows a perfect negative linear correlation between  $B$  and  $\gamma_{geom}$  having a steeper decreasing rate for lower look angles. Because  $\gamma_{baseline} = \gamma_{geom} \cdot \gamma_{vol}$ , according to Equation (9), one can admit that the higher the baseline, the lower  $\gamma_{baseline}$  and the higher  $\sigma_{\Delta\varphi}$ .

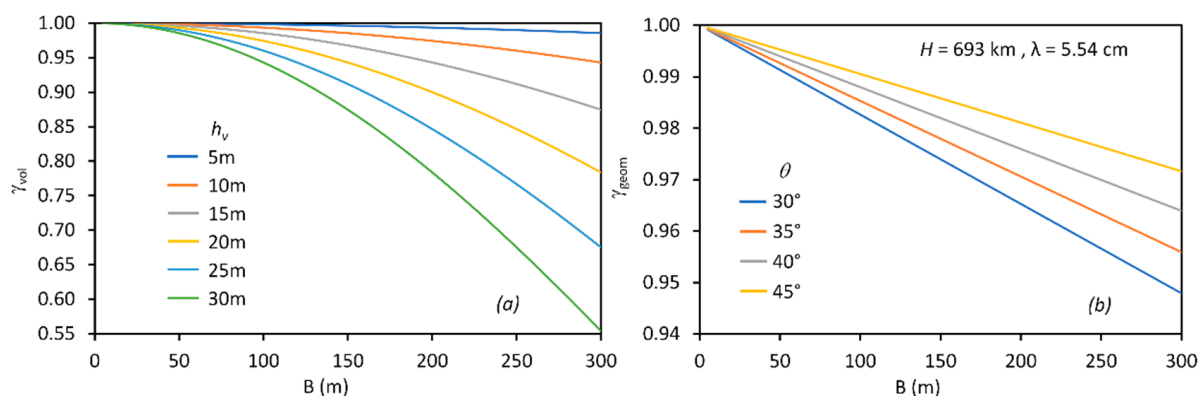


**Figure 4.** (a)  $\gamma_{vol}$  versus  $B$  and  $h_v$  ( $\theta = 35^\circ$ ). (b)  $\gamma_{geom}$  versus  $B$  and  $\theta$ .

### 3.3. Minimizing $\sigma_{dh}$ through Simulated Scenarios

According to Equation (12),  $\sigma_{d\Delta\varphi}$  depends on  $B$  and  $h_v$ . To explore its dependency,  $B$  and  $h_v$  were changed progressively from 5 m to 1000 m and from 5 m to 50 m, respectively, testing their effects on  $\sigma_{dh}$  (Figure 5a).

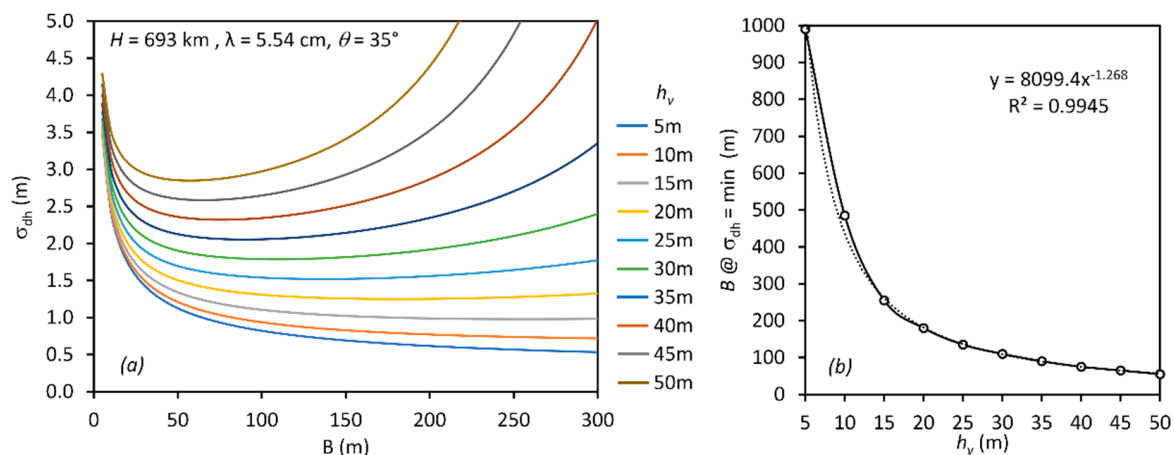


**Figure 5.** (a) Several scenarios of  $dh$  uncertainty according to  $h_v$  and  $B$ . (b) Power model relating  $h_v$  and  $B$  at  $dh$  uncertainty is minimized.

Simulations in Figure 5a show that  $h_v$  value  $> 15$  m (i.e., the majority of forests), and  $\sigma_{dh}$  presents a minimum with respect to  $B$ .

It is worth noting that  $\sigma_{dh}$  values are certainly underestimated. In fact,  $\gamma_{thermal}$ ,  $\gamma_{Doppler}$ ,  $\gamma_{temp}$  are factors that cannot be properly modelled, being independent from the features of interferometer.

Considering  $B$  values minimize  $\sigma_{dh}$  for the different  $h_v$  values, a model directly relating the “optimal”  $B$  value with the expected  $h_v$  was defined (Equation (13) and Figure 5b).

A simple power model can be calibrated (Equation (13)), as reported in Figure 5b (see figure for model  $a$ ,  $b$  and  $R^2$  coefficients). It is worth noting that the optimal  $B$  value occurs within the critical baseline (for S1, about 5 km) supporting the hypothesis that, over vegetation, the accuracy of interferometric-derived heights does not increase by using large baselines. The operational utility of this model can be easily exemplified using a case study. Suppose we investigate tree heights in a forest having an expected value of 25 m. The model of Figure 5b makes possible to obtain an optimal baseline value of 150 m. Similarly, it can be said that the optimal  $B$  value in forests with tree heights ranging between 15 m and 30 m (the majority of forest in temperate zones) should range between 250 m and 100 m, respectively.

Since pixel size (NL/SGRP) has been proved to significantly impact  $\sigma_{\Delta\phi}$ , and consequently  $\sigma_{d\Delta\phi}$  (Equation (9)), some simulations were performed to describe SGRP dependency from  $\gamma$  (Figure 6). Equations (14) and (15) were applied repeatedly assuming a reference  $\sigma_{dh} = 3$  m, and setting the following values for the involved parameters:  $H = 693$  km,  $\theta = 35^\circ$ , and  $\delta_{az} = 20$  m. This made it possible to describe SGRP variation against  $\gamma$  and  $B$ . Figure 6 shows that SGRP is inversely proportional to  $\gamma$ .

Since vegetation usually presents medium–low coherence values expected in the range  $0.2 < \gamma < 0.6$  [17], correspondent expected SGRP falls in the range 50–300 m if  $B > 50$  m. This SGRP (geometric resolution) is certainly not appropriate for a fine scale height retrieval; nevertheless, it appears to be proper for small-scale analysis (wide areas), generating a granularity that is consistent with the ones from traditional forest surveys. These are, in fact, characterized by a low-density of ground sampling (plots) [53].

Once the optimal  $B$  value was found and, consequently, the correspondent SGRP was found,  $\sigma_{dh}$  can be estimated as a function of  $\gamma_{FP}$  and expected  $dh$ . To investigate these dependencies, a simulation was run assuming baseline values in the range of 50–200 m using Equation (5) (Figure 7). During simulations, the following operational parameters were used:  $NL = 100$ ,  $\theta = 35^\circ$ , and  $H = 693$  km.

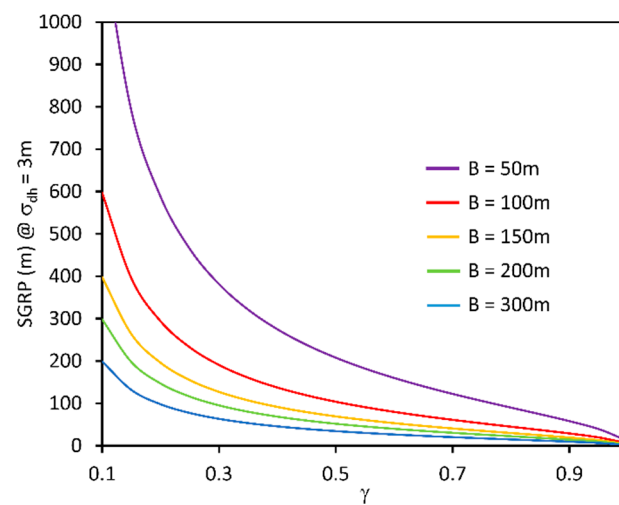


**Figure 6.** SGRP (squared pixel size) vs. coherence. A  $\sigma_{dh}$  equal to 3 m was used during simulations obtained by varying  $\gamma$  and  $B$ .

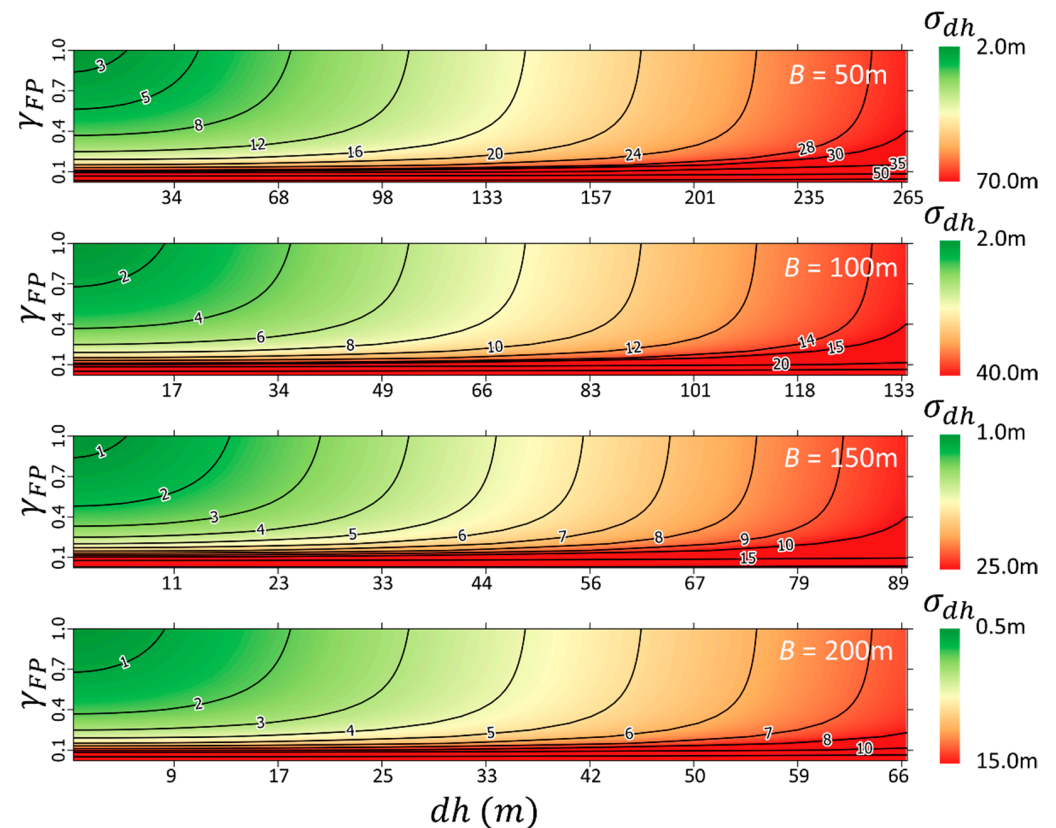


**Figure 7.** Several scenarios of  $dh$  uncertainty according to expected  $\gamma_{FP}$  and  $dh$  at different  $B$  values. Isolines refer to the same  $\sigma_{dh}$  values.

Figure 7 shows that  $dh$  values consistent with forest height in the range of 10–65 m generate  $\sigma_{dh}$  values varying between 1 m and 70 m, depending on  $\gamma_{FP}$  (coherence of the forest area) and  $B$  values. The most favourable conditions occur for high  $\gamma_{FP}$  and larger baselines. A focus point is that  $\sigma_{dh}$  remains at low values, while  $\gamma$  is higher than about 0.2, and can suddenly and significantly increase once this threshold is overcome. This suggests that a  $\gamma$  value of 0.2 can be somehow used to define significant/reliable measures.

In general, when  $dh$  tends to HOA,  $\sigma_{dh}$  is higher, suggesting that small  $dh$  values are more accurate than large ones. Operationally speaking, since the authors approach is based

on height difference computation, expected  $dh$  values (10–65 m) are always lower than HOA and result in a  $\sigma_{dh} < 5$  m. Some examples are reported in Table 3.

**Table 3.** Best cases from simulations in a typical Italian forest context (tree height in the range of 10–30 m).

<i>Baseline (m)</i>	<i>Expected dh (m)</i>	<i><math>\sigma_{dh}</math> (m)</i>
50	10–30	2
100	10–30	2
150	10–30	1
200	10–30	0.5

Similar results were found in [32,54] by using ERS-1 data where phase unwrapping was adopted. Otherwise, in the proposed approach, similar accuracy was found avoiding phase unwrapping, resulting into a more robust and controllable forest height uncertainty estimation. Moreover, values of Table 3 prove that forest height estimates from S1 InSAR data can generate results with an accuracy comparable to those of traditional surveys, making this technique an effective tool for forest structural monitoring.

Once more, this evidence highlights that an InSAR technique operated according to the above-mentioned optimization criteria can drive forest height estimates consistent with the ones found from ground surveys. Nevertheless, some limitations still persist concerning low coherence targets where InSAR fails to retrieve reliable forest height estimates [55]. It is worth stressing that these findings are based on simulations; therefore, future developments will be expected to sustain these deductions using real data and quantifying the actual (not the expected) errors in forest height retrieval.

#### 4. Conclusions

This work proved that S1 interferometric data can be effectively adopted to retrieve forest height. In particular, adopting the topographic levelling approach based on local differencing between interferograms from a forest pixel and a neighbour bare soil, one is permitted to operate with no phase unwrapping, resulting in an unambiguous height estimate. The authors proved that tuning the optimal baseline and multilooking factor can improve the accuracy of forest height retrieval. In particular, forest heights in the range of 10–30 m require an optimal baseline between 250 and 100 m. Furthermore, contrarily to the general rule that suggests large  $B$  values improve InSAR-derived DEM accuracy, this work demonstrates that, in forest areas, the same rule fails. In fact, by increasing  $B$ , forest coherence decreases, reducing interferometric phase accuracy. A simple model was additionally proposed and calibrated, aimed at predicting the optimal  $B$  value (and therefore image pair selection) for  $\sigma_{dh}$  minimization. Regarding the spatial density of forest height estimates, it was found that SGRP values between 50 and 100 m can guarantee a  $\sigma_{dh} < 3$  m. This resolution is certainly not appropriate for fine-scale analysis, suggesting the adoption of this method when small-scale (wide areas) mapping of forest heights is required. Finally, in this paper, authors proved that S1 InSAR data processed by focusing on height differencing computation (see Equation (2)) is effective in retrieving forest heights with medium–high accuracy. This has been necessarily achieved opportunely by tuning user-dependent parameters ( $B$ ,  $NL$ ,  $B_{temp}$ ) according to the above-mentioned maximization criteria.

**Author Contributions:** Conceptualization, S.D.P.; methodology, S.D.P.; software, F.S. and S.D.P.; validation, S.D.P. and F.S.; formal analysis, S.D.P. and F.S.; investigation, S.D.P. and F.S.; resources, S.D.P. and F.S.; data curation, S.D.P.; writing—original draft preparation, S.D.P. and F.S.; writing—review and editing, E.B.-M.; visualization, S.D.P. and F.S., supervision, E.B.-M. All authors have read and agreed to the published version of the manuscript.

**Funding:** This research received no external funding.

**Institutional Review Board Statement:** Not applicable.

**Informed Consent Statement:** Informed consent was obtained from all subjects involved in the study.

**Data Availability Statement:** Data sharing not applicable.

**Conflicts of Interest:** The authors declare no conflict of interest.

## References

- Segura, M.; Kanninen, M. Allometric Models for Tree Volume and Total Aboveground Biomass in a Tropical Humid Forest in Costa Rica. *Biotrop. J. Biol. Conserv.* **2005**, *37*, 2–8.
- Laurin, G.V.; Ding, J.; Disney, M.; Bartholomeus, H.; Herold, M.; Papale, D.; Valentini, R. Tree Height in Tropical Forest as Measured by Different Ground, Proximal, and Remote Sensing Instruments, and Impacts on above Ground Biomass Estimates. *Int. J. Appl. Earth Obs. Geoinf.* **2019**, *82*, 101899. [\[CrossRef\]](#)
- Hao, Z.; Zhang, J.; Song, B.; Ye, J.; Li, B. Vertical Structure and Spatial Associations of Dominant Tree Species in an Old-Growth Temperate Forest. *For. Ecol. Manag.* **2007**, *252*, 1–11. [\[CrossRef\]](#)
- Song, B.; Chen, J.; Desander, P.V.; Reed, D.D.; Bradshaw, G.A.; Franklin, J.F. Modeling Canopy Structure and Heterogeneity across Scales: From Crowns to Canopy. *For. Ecol. Manag.* **1997**, *96*, 217–229. [\[CrossRef\]](#)
- Spies, T.A. Forest Structure: A Key to the Ecosystem. *Northwest Sci.* **1998**, *72*, 34–36.
- Lund, H.G. When Is a Forest Not a Forest? *J. For.* **2002**, *100*, 21–28.
- Sillett, S.C.; Van Pelt, R.; Koch, G.W.; Ambrose, A.R.; Carroll, A.L.; Antoine, M.E.; Mifsud, B.M. Increasing Wood Production through Old Age in Tall Trees. *For. Ecol. Manag.* **2010**, *259*, 976–994. [\[CrossRef\]](#)
- Hanewinkel, M.; Hummel, S.; Albrecht, A. Assessing Natural Hazards in Forestry for Risk Management: A Review. *Eur. J. For. Res.* **2011**, *130*, 329–351. [\[CrossRef\]](#)
- Martins, A.C.; Willig, M.R.; Presley, S.J.; Marinho-Filho, J. Effects of Forest Height and Vertical Complexity on Abundance and Biodiversity of Bats in Amazonia. *For. Ecol. Manag.* **2017**, *391*, 427–435. [\[CrossRef\]](#)
- Bohn, F.J.; Huth, A. The Importance of Forest Structure to Biodiversity–Productivity Relationships. *R. Soc. Open Sci.* **2017**, *4*, 160521. [\[CrossRef\]](#)
- Bragg, D.C. Accurately Measuring the Height of (Real) Forest Trees. *J. For.* **2014**, *112*, 51–54. [\[CrossRef\]](#)
- Larsen, D.R.; Hann, D.W.; Stearns-Smith, S.C. Accuracy and Precision of the Tangent Method of Measuring Tree Height. *West. J. Appl. For.* **1987**, *2*, 26–28. [\[CrossRef\]](#)
- De Petris, S.; Berretti, R.; Sarvia, F.; Borgogno Mondino, E. When a Definition Makes the Difference: Operative Issues about Tree Height Measures from RPAS-Derived CHMs. *iFor.-Biogeosci. For.* **2020**, *13*, 404. [\[CrossRef\]](#)
- Hüttich, C.; Eberle, J.; Shvidenko, A.; Schepaschenko, D. Supporting a Forest Observation System for Siberia: Earth Observation for Monitoring, Assessing and Providing Forest Resource Information. Ecosystems 2014. Available online: <https://earthzine.org/supporting-a-forest-observation-system-for-siberia-earth-observation-for-monitoring-assessing-and-providing-forest-resource-information/> (accessed on 27 February 2022).
- Goldstein, R.M.; Zebker, H.A.; Werner, C.L. Satellite Radar Interferometry: Two-Dimensional Phase Unwrapping. *Radio Sci.* **1988**, *23*, 713–720. [\[CrossRef\]](#)
- Chen, C.W.; Zebker, H.A. Phase Unwrapping for Large SAR Interferograms: Statistical Segmentation and Generalized Network Models. *IEEE Trans. Geosci. Remote Sens.* **2002**, *40*, 1709–1719. [\[CrossRef\]](#)
- Braun, A. Retrieval of Digital Elevation Models from Sentinel-1 Radar Data—Open Applications, Techniques, and Limitations. *Open Geosci.* **2021**, *13*, 532–569. [\[CrossRef\]](#)
- Hagberg, J.O.; Ulander, L.M.; Askne, J. Repeat-Pass SAR Interferometry over Forested Terrain. *IEEE Trans. Geosci. Remote Sens.* **1995**, *33*, 331–340. [\[CrossRef\]](#)
- Santoro, M.; Askne, J.; Dammert, P.B. Tree Height Influence on ERS Interferometric Phase in Boreal Forest. *IEEE Trans. Geosci. Remote Sens.* **2005**, *43*, 207–217. [\[CrossRef\]](#)
- Romero-Puig, N.; Lopez-Sanchez, J.M. A Review of Crop Height Retrieval Using InSAR Strategies: Techniques and Challenges. *IEEE J. Sel. Top. Appl. Earth Obs. Remote Sens.* **2021**, *14*, 7911–7930. [\[CrossRef\]](#)
- De Petris, S.; Sarvia, F.; Gullino, M.; Tarantino, E.; Borgogno-Mondino, E. Sentinel-1 Polarimetry to Map Apple Orchard Damage after a Storm. *Remote Sens.* **2021**, *13*, 1030. [\[CrossRef\]](#)
- Sarvia, F.; Xausa, E.; De Petris, S.D.; Cantamessa, G.; Borgogno-Mondino, E. A Possible Role of Copernicus Sentinel-2 Data to Support Common Agricultural Policy Controls in Agriculture. *Agronomy* **2021**, *10*, 110. [\[CrossRef\]](#)
- De Petris, S.; Sarvia, F.; Borgogno-Mondino, E. Multi-Temporal Mapping of Flood Damage to Crops Using Sentinel-1 Imagery: A Case Study of the Sesia River (October 2020). *Remote Sens. Lett.* **2021**, *12*, 459–469. [\[CrossRef\]](#)
- Vollrath, A.; Mullissa, A.; Reiche, J. Angular-Based Radiometric Slope Correction for Sentinel-1 on Google Earth Engine. *Remote Sens.* **2020**, *12*, 1867. [\[CrossRef\]](#)
- Reiche, J.; Lucas, R.; Mitchell, A.L.; Verbesselt, J.; Hoekman, D.H.; Haarpaintner, J.; Kelndorfer, J.M.; Rosenqvist, A.; Lehmann, E.A.; Woodcock, C.E. Combining Satellite Data for Better Tropical Forest Monitoring. *Nat. Clim. Chang.* **2016**, *6*, 120–122. [\[CrossRef\]](#)



26. Veci, L. *SENTINEL-1 Toolbox SAR Basics Tutorial*; ARRAY Systems Computing, Inc.; European Space Agency: Paris, France, 2015.
27. Garestier, F.; Dubois-Fernandez, P.C.; Papathanassiou, K.P. Pine Forest Height Inversion Using Single-Pass X-Band PolInSAR Data. *IEEE Trans. Geosci. Remote Sens.* **2007**, *46*, 59–68. [\[CrossRef\]](#)
28. Managhebi, T.; Maghsoudi, Y.; Zoej, M.J.V. A Volume Optimization Method to Improve the Three-Stage Inversion Algorithm for Forest Height Estimation Using PolInSAR Data. *IEEE Geosci. Remote Sens. Lett.* **2018**, *15*, 1214–1218. [\[CrossRef\]](#)
29. Cloude, S.R.; Chen, H.; Goodenough, D.G. Forest Height Estimation and Validation Using Tandem-X Polinsar. In Proceedings of the 2013 IEEE International Geoscience and Remote Sensing Symposium-IGARSS, Melbourne, VIC, Australia, 21–26 July 2013; pp. 1889–1892.
30. Soja, M.J.; Persson, H.; Ulander, L.M. Estimation of Forest Height and Canopy Density from a Single InSAR Correlation Coefficient. *IEEE Geosci. Remote Sens. Lett.* **2014**, *12*, 646–650. [\[CrossRef\]](#)
31. Askne, J.; Santoro, M. Multitemporal Repeat Pass SAR Interferometry of Boreal Forests. *IEEE Trans. Geosci. Remote Sens.* **2005**, *43*, 1219–1228. [\[CrossRef\]](#)
32. Askne, J.I.; Dammert, P.B.; Ulander, L.M.; Smith, G. C-Band Repeat-Pass Interferometric SAR Observations of the Forest. *IEEE Trans. Geosci. Remote Sens.* **1997**, *35*, 25–35. [\[CrossRef\]](#)
33. Ainsworth, T.L.; Kelly, J.; Lee, J.-S. Polarimetric Analysis of Dual Polarimetric SAR Imagery. In Proceedings of the 7th European Conference on Synthetic Aperture Radar, Friedrichshafen, Germany, 2–5 June 2008; pp. 1–4.
34. Geudtner, D.; Torres, R.; Snoeij, P.; Davidson, M.; Rommen, B. Sentinel-1 System Capabilities and Applications. In Proceedings of the 2014 IEEE Geoscience and Remote Sensing Symposium, Quebec City, QC, Canada, 13–18 July 2014; pp. 1457–1460.
35. Torres, R.; Snoeij, P.; Geudtner, D.; Bibby, D.; Davidson, M.; Attema, E.; Potin, P.; Rommen, B.; Floury, N.; Brown, M. GMES Sentinel-1 Mission. *Remote Sens. Environ.* **2012**, *120*, 9–24. [\[CrossRef\]](#)
36. Small, D.; Schubert, A. *Guide to Sentinel-1 Geocoding 2019*; University of Zurich: Zurich, Switzerland, 2019.
37. Attema, E.; Davidson, M.; Snoeij, P.; Rommen, B.; Floury, N. Sentinel-1 Mission Overview. In Proceedings of the 2009 IEEE International Geoscience and Remote Sensing Symposium, Cape Town, South Africa, 12–17 July 2009; Volume 1, pp. 1–36.
38. Li, F.K.; Goldstein, R.M. Studies of Multibaseline Spaceborne Interferometric Synthetic Aperture Radars. *IEEE Trans. Geosci. Remote Sens.* **1990**, *28*, 88–97. [\[CrossRef\]](#)
39. Rodriguez, E.; Martin, J.M. Theory and Design of Interferometric Synthetic Aperture Radars. *IEE Proc. F Radar Signal Process.* **1992**, *139*, 147–159. [\[CrossRef\]](#)
40. Richards, J.A. *Remote Sensing with Imaging Radar*; Springer: Berlin/Heidelberg, Germany, 2009; Volume 1.
41. Clancy, J. *Site Surveying and Levelling*; Routledge: London, UK, 2013.
42. Hanssen, R.F. *Radar Interferometry: Data Interpretation and Error Analysis*; Springer Science & Business Media: Berlin/Heidelberg, Germany, 2001; Volume 2.
43. Hughes, I.; Hase, T. *Measurements and Their Uncertainties: A Practical Guide to Modern Error Analysis*; OUP Oxford: Oxford, UK, 2010.
44. Pepe, A.; Calò, F. A Review of Interferometric Synthetic Aperture RADAR (InSAR) Multi-Track Approaches for the Retrieval of Earth's Surface Displacements. *Appl. Sci.* **2017**, *7*, 1264. [\[CrossRef\]](#)
45. Ferretti, A.; Monti-Guarnieri, A.V.; Prati, C.M.; Rocca, F.; Massonnet, D. *INSAR Principles B*; ESA Publications: Noordwijk, The Netherlands, 2007.
46. Zebker, H.A.; Villasenor, J. Decorrelation in Interferometric Radar Echoes. *IEEE Trans. Geosci. Remote Sens.* **1992**, *30*, 950–959. [\[CrossRef\]](#)
47. Yagüe-Martínez, N.; Prats-Iraola, P.; Gonzalez, F.R.; Bricic, R.; Shau, R.; Geudtner, D.; Eineder, M.; Bamler, R. Interferometric Processing of Sentinel-1 TOPS Data. *IEEE Trans. Geosci. Remote Sens.* **2016**, *54*, 2220–2234. [\[CrossRef\]](#)
48. Qin, Y.; Perissin, D.; Bai, J. Investigations on the Coregistration of Sentinel-1 TOPS with the Conventional Cross-Correlation Technique. *Remote Sens.* **2018**, *10*, 1405. [\[CrossRef\]](#)
49. Jung, J.; Kim, D.; Laval, M.; Yun, S.-H. Coherent Change Detection Using InSAR Temporal Decorrelation Model: A Case Study for Volcanic Ash Detection. *IEEE Trans. Geosci. Remote Sens.* **2016**, *54*, 5765–5775. [\[CrossRef\]](#)
50. Ahmed, R.; Siqueira, P.; Hensley, S.; Chapman, B.; Bergen, K. A Survey of Temporal Decorrelation from Spaceborne L-Band Repeat-Pass InSAR. *Remote Sens. Environ.* **2011**, *115*, 2887–2896. [\[CrossRef\]](#)
51. Santoro, M.; Shvidenko, A.; McCallum, I.; Askne, J.; Schumliuss, C. Properties of ERS-1/2 Coherence in the Siberian Boreal Forest and Implications for Stem Volume Retrieval. *Remote Sens. Environ.* **2007**, *106*, 154–172. [\[CrossRef\]](#)
52. Gisinger, C.; Schubert, A.; Breit, H.; Garthwaite, M.; Balss, U.; Willberg, M.; Small, D.; Eineder, M.; Miranda, N. In-Depth Verification of Sentinel-1 and TerraSAR-X Geolocation Accuracy Using the Australian Corner Reflector Array. *IEEE Trans. Geosci. Remote Sens.* **2020**, *59*, 1154–1181. [\[CrossRef\]](#)
53. Wagner, F.; Rutishauser, E.; Blanc, L.; Herault, B. Effects of Plot Size and Census Interval on Descriptors of Forest Structure and Dynamics. *Biotropica* **2010**, *42*, 664–671. [\[CrossRef\]](#)
54. Dammert, P.B. Accuracy of INSAR Measurements in Forested Areas. In *ERS SAR Interferometry, Proceedings of the Fringe 96 Workshop, Zurich, Switzerland, 30 September–2 October 1996*; European Space Agency: Paris, France, 1997; Volume 406, p. 37.
55. Askne, J.; Dammert, P.B.; Smith, G. Interferometric SAR Observations of Forested Areas. In Proceedings of the Third ERS Symposium on Space at the Service of Our Environment, Florence, Italy, 17–21 March 1997; Volume 414, p. 337.